Improvement of Superplasticity in High-Mg Aluminum Alloys by Sacrifice of Some Room Temperature Formability

H. JIN, B. SHALCHI AMIRKHIZ, and D.J. LLOYD

The mechanical properties of fully annealed Al-4.6 wt pct Mg alloys with different levels of Mn and Fe have been characterized at room and superplastic forming (SPF) temperatures. The effects of Mn and Fe on the intermetallic phase, grain structure, and cavitation were investigated and correlated to the formability at different temperatures. Although both Mn and Fe contribute to the formation of $Al_6(Mn,Fe)$ phase, which refines the grain structure by particle-stimulated nucleation and Zener pinning, their effects are different. An increasing Mn reduces the room temperature formability due to the increasing number of intermetallic particles, but significantly improves the superplasticity by fine grain size-induced grain boundary sliding. Meanwhile, the Fe makes the constituent particles very coarse, resulting in reduced formability at all temperatures due to extensive cavitation. A combination of high Mn and low Fe is therefore beneficial to SPF, while low levels of both elements are good for cold forming. Consequently, the superplasticity of high-Mg aluminum alloys can be significantly improved by modifying the chemical composition with sacrifice of some room temperature formability.

https://doi.org/10.1007/s11661-018-4546-y

I. INTRODUCTION

ALUMINUM alloys with high-Mg content, such as AA5083, are widely used as structural materials in ship building, automotive, aircraft, and other manufacturing industries. These alloys were initially designed to supply as fully annealed (*e.g.*, O temper) or near-fully annealed (*e.g.*, H32 temper) sheet products for cold forming, so the chemical compositions were optimized for balanced strength and formability at room temperature. They usually contain 4.0 to 4.9 pct Mg, 0.4 to 1.0 pct Mn, 0.2 to 0.3 pct Fe, and very low Si (all in wt pct hereinafter). The 4.0 to 4.9 pct Mg gives nearly the maximum solid solution hardening effect without causing serious technical issues, such as hot tearing, edge cracking, and reduction in corrosion resistance.[1–4] Manganese is added for grain size control, providing grain boundary hardening, and preventing orange peeling upon forming, but it is usually kept below 1 pct to avoid significant reduction of room temperature formability.[5] The Fe and Si are the most common impurity elements, coming from Bauxite, recycled aluminum scraps, and steel tools used in the smelter and cast house. The Fe is usually controlled around 0.2 to 0.3 pct, while higher level damages the formability and lower one increases the material cost. Since Si forms Mg_2Si phase and thus reduces the Mg in solid solution, it is tightly controlled at 0.1 pct or below.

High-Mg aluminum alloys are also supplied in heavily cold-rolled condition (*e.g.*, H18 temper) for superplastic forming (SPF).[6–11] In SPF of these alloys the work piece is heated up in minutes to the desired forming temperature at 425 °C to 525 °C, while a uniform fine grain structure is generated. The fine grain structure enables grain boundary sliding and thus leads to extended plasticity. The extended plasticity in high-Mg aluminum alloys is often not prominent, because the grain size is not fine enough to fully realize the potential of high temperature formability. For example, for commercial AA5083 H18 sheet products under typical SPF condition, the mean grain size is 15 to 20 μm and the maximum tensile elongation is around 300 to 350 pct. Meanwhile, the famous Al-6 pct Cu-0.5 pct Zr Supral 100 alloy, which was specifically designed for SPF for aerospace applications, is able to maintain a mean grain size below 5 μm and to reach more than 1000 pct tensile elongation.[12–14]

H. JIN and B. SHALCHI AMIRKHIZ are with the CanmetMATERIALS, Natural Resources Canada, Hamilton, ON L8P 0A5, Canada. Contact e-mail: haiou.jin@canada.ca D.J. LLOYD is with Aluminum Materials Consultants, Bath, ON K0H 1G0 Canada.

Manuscript submitted July 31, 2017.
Article published online March 9, 2018

Nevertheless, the aluminum products having true superplasticity are usually very expensive, because they often contain expensive alloying elements, *e.g.*, Sc and Zr,[15,16] and/or are fabricated through complex processing routes with additional overaging.[17, 18] Moreover, many products specifically developed for SPF are metal matrix composites,[19,20] eutectic alloys,[21,22] or regular alloys but processed by severe plastic deformation,[23–25] whereas the material and processing costs are much higher than regular sheet products. The conventional high-Mg alloys such as AA5083 are therefore still widely used as inexpensive SPF materials. Although high temperature performance was not considered in the initial alloy design, there might be potential to improve the superplasticity for these alloys without additives of expensive alloying elements or using complex processing routes. In the present work, the effects of major alloying element Mn and major impurity element Fe on the mechanical properties of Al-4.6 pct Mg were systematically studied at room and SPF temperatures. It was attempted to improve the superplasticity by modifying the Mn and Fe levels, without adding other alloying elements or changing the commercial sheet processing route.

II. EXPERIMENTS

Nine Al-4.6 pct Mg alloys with 0.5 to 1.5 pct Mn and 0.05 to 0.27 pct Fe, labeled as Alloys-1 to 9, were made by DC casting on a 95.25 × 228.6 mm conventional aluminum mold (Table I). The casting temperature in the basin was 700 ± 5 °C, and the casting speed was 100 mm/min with a water flow rate of 90 L/min. The 95-mm-thick as-cast ingots were scalped by ~ 10 mm on each rolling face, re-heated to 540 °C, homogenized for 5 to 6 hours, hot rolled to ~ 8 mm with exit temperature at 275 °C to 300 °C, and cold rolled down to the final gauge of ~ 1.5 mm to reach the H18 temper. All the alloys have more or less some edge cracking during hot and cold rolling depending on the Mn and/or Fe levels. In hot rolling, the tendency to edge cracking appears independent of Mn, but increases significantly with the increasing Fe level. Meanwhile, the tendency to edge cracking in cold rolling increases whenever Mn or Fe levels increase. The samples for room temperature mechanical testing were batch annealed at 350 °C for 2 hours with a very low heating rate, 50 °C/h, to obtain the fully recrystallized O temper, while those for high temperature tensile testing remain in the H18 temper. To investigate the thermal stability of grain structure at high temperatures, coupon-sized H18 specimens were flash annealed at 475 °C, 500 °C, and 525 °C for 5 to 60 minutes in a pre-heated small air furnace followed by forced air quench. Both the heating-up and cooling-down of the specimen were completed within 1 minute.

Table I. The Chemical Compositions of High-Mg Aluminum Ingots (in Weight Percent)

Alloy	Fe	Mg	Mn	Si	Al
1	0.04	4.53	0.52	0.03	balance
2	0.05	4.62	0.99	0.03	balance
3	0.05	4.61	1.44	0.04	balance
4	0.14	4.52	0.51	0.06	balance
5	0.16	4.62	0.99	0.06	balance
6	0.18	4.67	1.48	0.07	balance
7	0.26	4.51	0.51	0.06	balance
8	0.27	4.61	0.95	0.06	balance
9	0.28	4.67	1.45	0.06	balance

The microstructures were characterized by Olympus PMG3 optical microscope, Philips XL30 scanning electron microscope (SEM), and FEI Tecnai Osiris transmission electron microscope (TEM) equipped with X-FEG gun and SuperEDS. All the grain size measurement was done in the sheet longitudinal section defined by rolling direction (RD) and thickness direction by line intercept method on SEM backscatter images. The optical and SEM specimens were prepared by mechanical polishing in the longitudinal section with diamond paste down to 1μm, followed by a mechanical-chemical polish using 0.5 μm colloidal silica for a few minutes. TEM foils were prepared in the planar plane defined by RD and transverse direction near the sheet center by electropolish in a 30 pct nitric acid in 70 pct methanol solution at 15 V and around − 30 °C.

For each alloy at H18 temper, the area density, size, and volume fraction of relatively large particles were determined by quantitative image analysis on the SEM secondary electron images taken in the longitudinal section through the entire thickness. The scanned area covers a total of 0.17 to 0.21 mm^2 and thousands of intermetallic particles over 0.5 μm were counted. The area density refers to the number of particles per unit area scanned, and the size is represented by the maximum Feret parameter (F_{max}), which is the longest axis of a particle. The smaller particles were investigated by TEM at 200 kV in STEM mode using bright field (BF) and high angle annular dark field (HAADF) detectors in combination with Energy-dispersive X-ray spectroscopy (EDS). The HAADF images contain chemical information as scattering at higher angles is related to the atomic Z-number. The EDS elemental mapping was done using ESPRIT software, and deconvolution of overlapping peaks was applied. The spatial resolution in elemental mapping is as high as 1 nm, depending on Z-number and thickness. For each alloy the examined area is 100 to 300 μm^2, and the thickness of the area is 40 to 300 nm.

The mechanical properties at room temperature were determined by tensile testing and wrap bend testing. The tensile testing was done in an Instron 5967 tensile machine with a constant cross-head speed equivalent to 6×10^{-4} s^{-1} initial strain rate. All the tensile specimens were machined along the RD with 19.05 mm gauge length and 12.7 mm gauge width, for testing at both room and high temperatures. Three specimens were tested and the average values of yield strength (YS), ultimate tensile strength (UTS), and total elongation (EL) were recorded. The specimens for wrap bend testing were cut along the transverse direction (TD) and

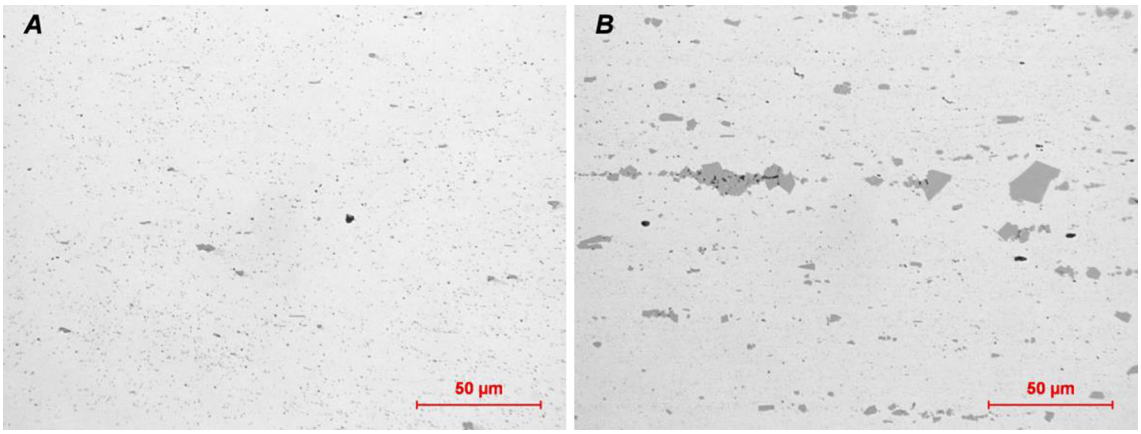

Fig. 1—Optical micrographs showing the intermetallic particles in the longitudinal section of final gauge sheets, (*a*) Alloy-1 with lowest Mn and Fe, and (*b*) Alloy-9 with highest Mn and Fe. The RD is horizontal.

wrapped around the mandrels with a series of radii from the large to the small. The wrap bendability is quantified by a parameter, $\frac{r}{t}$, where r is the minimum radius of mandrel that the specimen can be bent around without cracking and t is the specimen thickness. A lower $\frac{r}{t}$ value indicates better formability.

The high temperature tensile testing was performed at 425 °C to 525 °C with a constant cross-head speed corresponding to an initial strain rate at 2×10^{-3} s^{-1}, in an air chamber controlled by Zwick/Roell universal 3-zone furnace controller. Three thermocouples were used to control the heating rate and to enable uniform temperature in the specimen: two welded on the top and bottom grips and one attached on the center of specimen. The heating rate was set to be 7 °C/min, but when approaching the desired temperature it slowed down to avoid overshooting. It took ~ 2 hours to reach and stabilize at the testing temperature. For each testing condition 3 to 5 specimens were stretched to fracture but only the mechanical properties of the one with the highest EL were counted. The grain structures in the specimen end and specimen gauge near the fracture were examined after testing. To investigate the nucleation and growth of cavities, the specimens after stretching were cut in different locations with different levels of reduction-in-area. The volume fraction of cavities was estimated by quantitative image analysis covering an area of ~ 1.66 mm^2 through the thickness in optical micrographs taken in the cross sections.

III. RESULTS

A. *Intermetallic Particles*

In the final gauge sheets nearly all the particles analyzed by energy-dispersive X-ray in SEM are the $Al_6(Mn,Fe)$ phase, but a few very small Mg_2Si particles have also been detected. There are two types of $Al_6(Mn,Fe)$ phase: the coarse blocky or irregular-shaped constituents with particle size from several to several ten micrometers, and the relatively small rod-shaped submicron dispersoids. As shown in Figure 1, the small dispersoids are more or less evenly distributed, but the coarse constituents often segregate along the RD, especially when both Mn and Fe are high. The results of image analysis of coarse particles are shown in Table II, and the particle density as a function of particle size, in Figure 2. For the particles over 0.5 μm, an increasing Mn increases the density and volume fraction but reduces the particle size, while Fe increases the particle size and volume fraction but reduces the density (Figure 3).

Table II. The Density, Size, and Volume Fraction of $Al_6(Mn,Fe)$ Intermetallic Particles with F_{max} Over 0.5 μm, as well as the Calculated Grain Size Assuming Site-Saturated Nucleation

Alloy	Particle density (mm^{-2})	Mean particle size d_{PSN} (F_{max}) (μm)	Volume fraction F_V (Percent)	Grain size D_{PSN} (μm)
1	9934	1.22	0.55	6.9
2	37555	0.88	1.49	3.6
3	67008	0.99	2.93	3.2
4	7627	1.37	0.85	6.7
5	20390	1.15	1.64	4.5
6	39419	0.99	2.54	3.4
7	8182	1.63	1.34	6.9
8	17662	1.38	2.12	5.0
9	30719	1.19	3.11	3.8

For each alloy in H18 temper, about 60 to 300 relatively small secondary phase particles were analyzed by TEM, including $Al_6(Mn,Fe)$, α-$Al_{15}(Mn,Fe)_3Si_2$, Mg_2Si, and Si dispersoids while $Al_6(Mn,Fe)$ is dominant. As shown in Figure 4, the $Al_6(Mn,Fe)$ dispersoid particles are usually rod-shaped and ~ 0.1 to 1 μm in length, while the Mg_2Si and Si particles are spherical or oval with diameters around 0.1 to 0.2 μm. The α-$Al_{15}(Mn,Fe)_3Si_2$ particles are mostly observed in Alloys-1, 4, and 7, where the Mn level is only 0.5 pct. They could be spherical or blocky, and the particle size is usually submicron (Figure 5). As shown in Figure 6, many rod-shaped $Al_6(Mn,Fe)$ particles have very fine spherical voids in the ends of long axis, where local

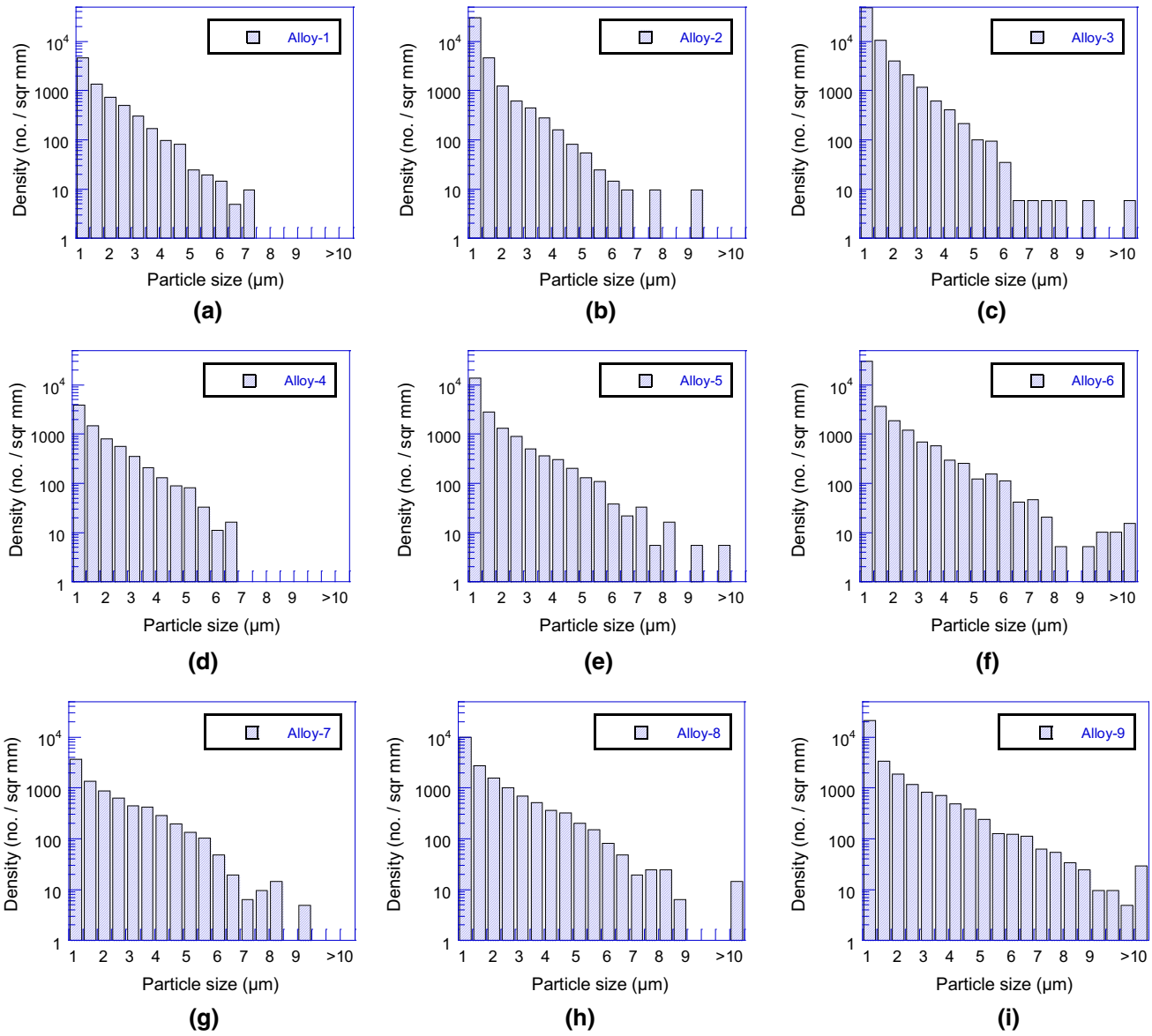

Fig. 2—The number of particles per mm^2 as a function of the particle size, (*a*) Alloy-1 with 0.52 pct Mn and 0.04 pct Fe, (*b*) Alloy-2 with 0.99 pct Mn and 0.05 pct Fe, (*c*) Alloy-3 with 1.44 pct Mn and 0.05 pct Fe, (*d*) Alloy-4 with 0.51 pct Mn and 0.14 pct Fe, (*e*) Alloy-5 with 0.99 pct Mn and 0.16 pct Fe, (*f*) Alloy-6 with 1.48 pct Mn and 0.18 pct Fe, (*g*) Alloy-7 with 0.51 pct Mn and 0.26 pct Fe, (*h*) Alloy-8 with 0.95 pct Mn and 0.27 pct Fe, and (*i*) Alloy-9 with 1.45 pct Mn and 0.28 pct Fe.

strain concentration may occur. The diameter of the spherical voids is similar to or smaller than the width of the rod, mostly below 100 nm. Some rod-shaped particles are broken, but voids are not always observed in the gaps.

Since by TEM it is very difficult to cover a large volume and count a high number of particles, no attempts were made to give the quantitative particle analysis the same as that shown in Table II and Figure 2. However, it is a general observation that the volume fraction of small particles increases with increasing Mn, *e.g.*, see Figure 7. It is unclear how impurity element Fe affects the volume fraction of small particles, but it appears the Fe is much more effective in controlling the size of coarse constituents than small dispersoids. It is difficult to conclude a relationship between the dispersoid particle size and the levels of Mn or Fe, but there is no obvious evidence that the mean particle size of the rod-shaped $Al_6(Mn,Fe)$ dispersoids is significantly increased with the increasing Mn and/or Fe levels.

B. *Grain Structures*

The grain structures in the O temper are uniform and equiaxed, having a decreasing grain size with increasing Mn and/or Fe (Table III and Figure 8). After flash annealing at 475 °C to 525 °C, only Alloy-1 having the lowest levels of both Mn and Fe shows abnormal grain growth, while the others are able to maintain a uniform, equiaxed, and small grain structure. The grains in Alloy-1 after abnormal grain growth are as coarse as

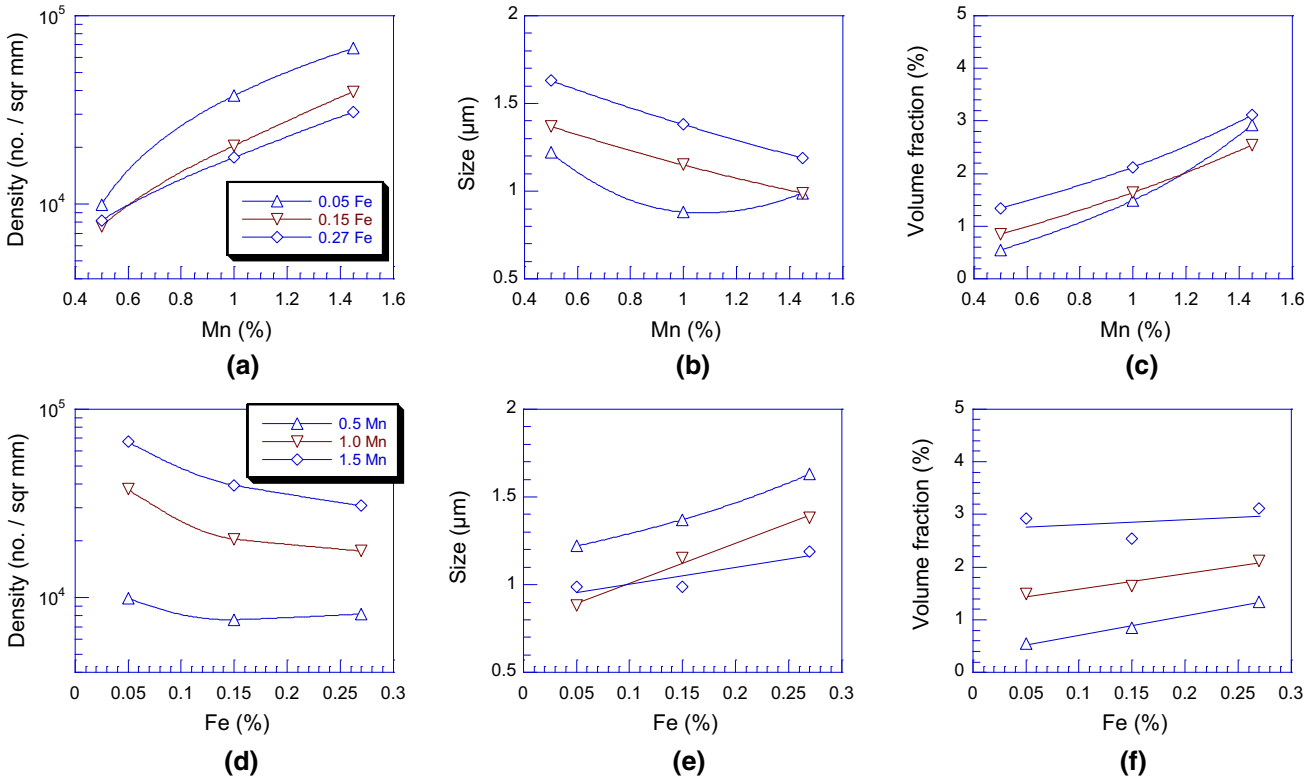

Fig. 3—The density, size, and volume fraction of the particles with F_{max} over 0.5 μm as a function of the Mn and Fe levels, (*a*) to (*c*) density, size, and volume fraction *vs* Mn, and (*d*) to (*f*) density, size, and volume fraction *vs* Fe.

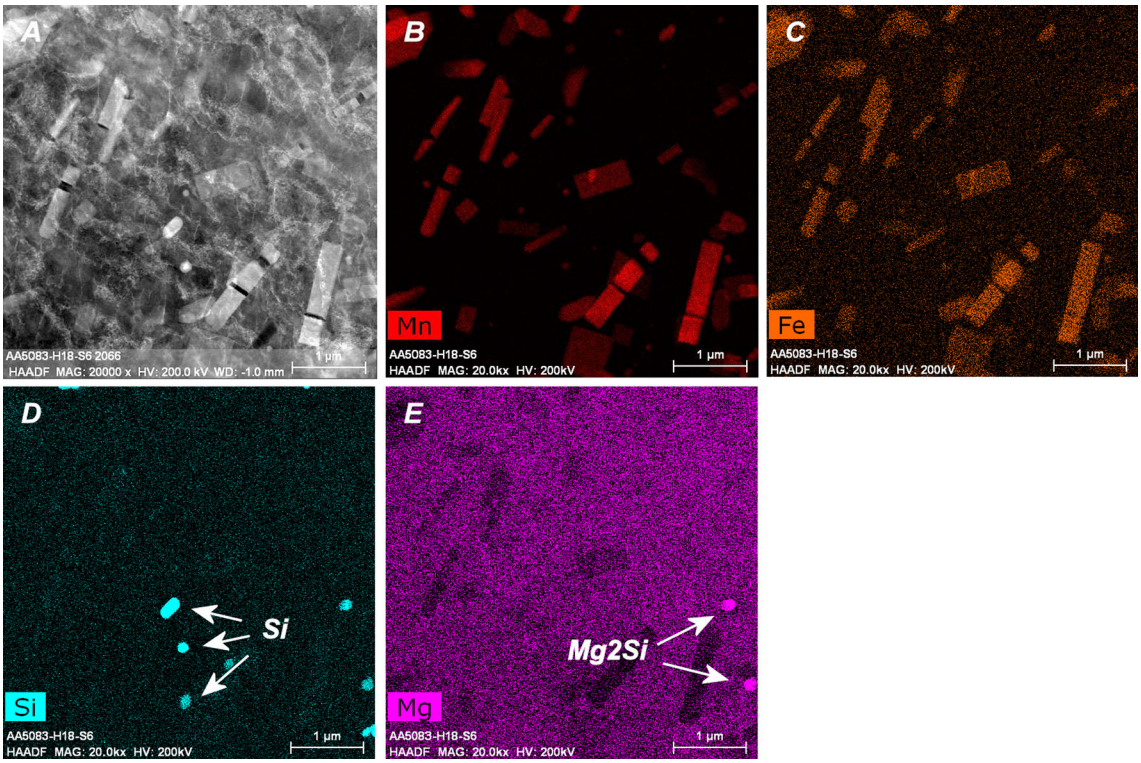

Fig. 4—TEM images showing the $Al_6(Mn,Fe)$, Si, and Mg_2Si particles in Alloy-6 H18 with 1.48 pct Mn and 0.18 pct Fe, (*a*) HAADF image, (*b*) to (*e*) element maps of Mn, Fe, Si, and Mg. The foil thickness of the mapped region is ~ 300 nm.

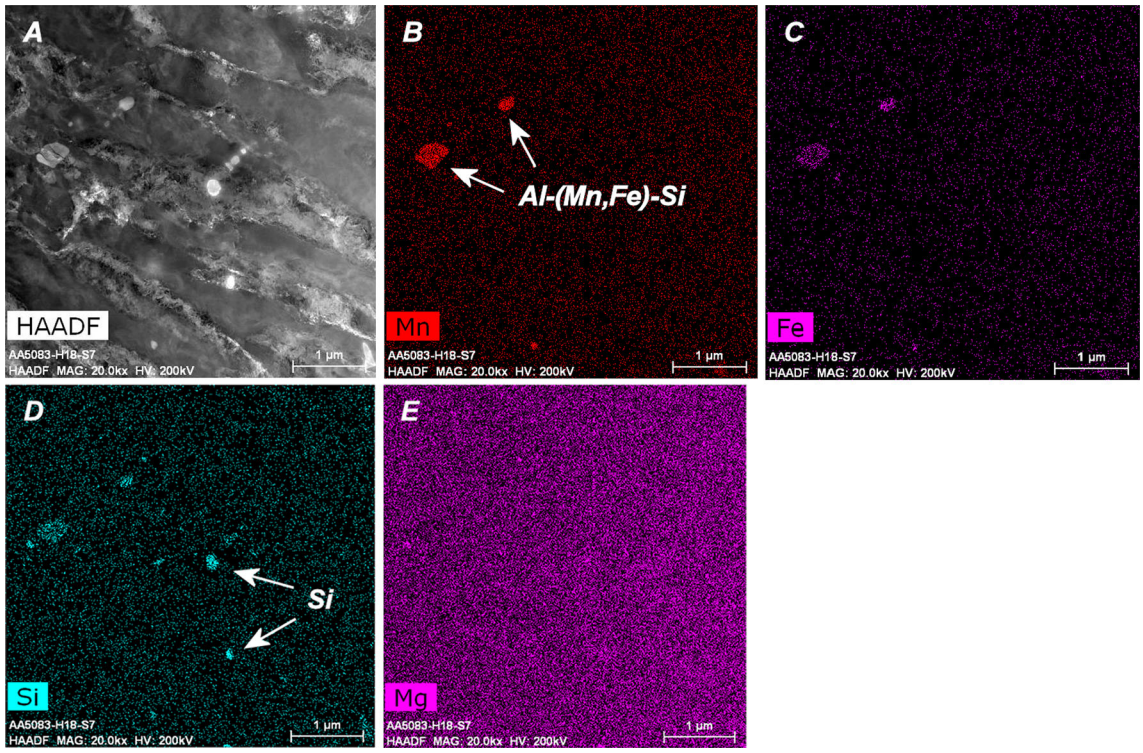

Fig. 5—TEM images showing the α-$Al_{15}(Mn,Fe)_3Si_2$ and Si particles in Alloy-7 H18 with 0.51 pct Mn and 0.26 pct Fe, (*a*) HAADF image, (*b*) to (*e*) element maps of Mn, Fe, Si, and Mg. The foil thickness of the mapped region is ~ 140 nm.

Fig. 6—TEM micrograph of Alloy-5 H18 with 0.99 pct Mn and 0.16 pct Fe showing a rod-shaped $Al_6(Mn,Fe)$ dispersoid with a void generated in the end of long axis.

~ 1 mm. For the remaining alloys, although the grain size increases with annealing time, it is stabilized after 30 minutes (Figure 9). Figure 10 shows the stabilized grain size as a function of Mn and Fe levels, revealing that the grain refinement effect from Mn is very strong, but that from Fe is prominent only when the Mn is very low.

Table IV lists the mean grain sizes after high temperature tensile testing in the specimen end parts, which were annealed only, and Table V, the ones in the specimen gauge parts near fracture, which were annealed and strained concurrently. The grain structure in the specimen end is very close to the stabilized grain structure after flash annealing at the same temperature. However, in the specimen gauge part, dynamic abnormal grain growth happens not only in Alloy-1 but also in Alloys-4 and 7, leading to the very coarse grain size in mm scale. For the remaining alloys the grain sizes are similar to those in the specimen ends, indicating that dynamic grain growth is not prominent.

C. *Room Temperature Properties*

The room temperature mechanical properties of the O temper sheets are listed in Table III. As shown in Figure 11, an increasing Mn improves the strength but reduces the EL, both significantly. Since the variation of Fe is in a narrow range, 0.05 to 0.27 pct, the relationship between tensile properties and Fe level is not very obvious. The YS and UTS increase slightly with increasing Fe when the Mn is low, but they decrease a little when Mn is high. The EL shows a general decreasing tendency with increasing Fe. Figure 12 shows that the wrap bendability decreases drastically with increasing Mn and/or Fe, especially when both elements are high.

D. *High Temperature Properties*

All the high temperature tensile properties are collected in Tables VI, VII, and VIII. As shown in

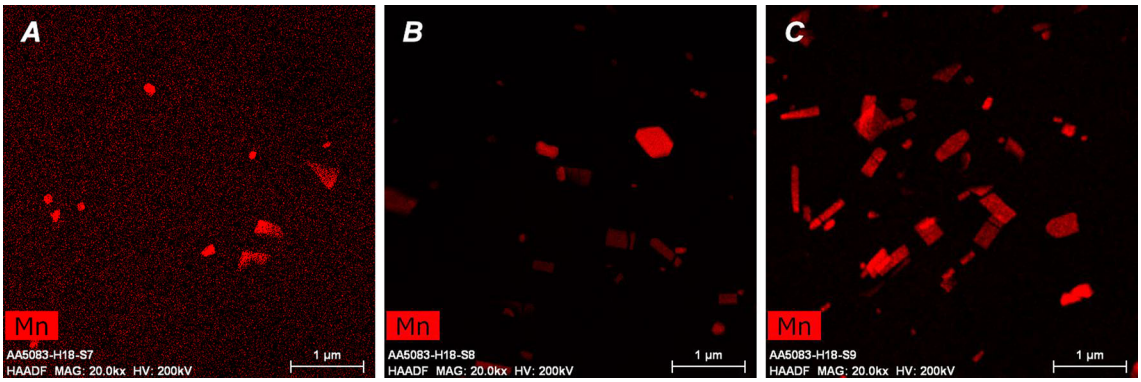

Fig. 7—The Mn-containing dispersoid particles in H18 sheets with increasing Mn, (*a*) Alloy-7 with 0.51 pct Mn and 0.26 pct Fe, (*b*) Alloy-8 with 0.95 pct Mn and 0.27 pct Fe, and (*c*) Alloy-9 with 1.45 pct Mn and 0.28 pct Fe.

Table III. The Measured Mean Grain Sizes and Room Temperature Mechanical Properties in the O Temper Sheets

Alloy	D (μm)	YS (MPa)	UTS (MPa)	EL (Percent)	r/t
1	13.6	156.7	311.3	31.7	0.19
2	10.8	173.0	344.5	24.0	0.26
3	10.0	193.0	365.0	22.0	0.38
4	11.4	162.0	314.3	26.0	0.20
5	10.7	176.0	347.0	25.0	0.32
6	9.9	186.7	362.0	20.0	0.46
7	10.5	164.7	316.0	27.3	0.26
8	10.2	176.0	341.3	25.3	0.38
9	9.3	187.7	357.0	21.0	0.63

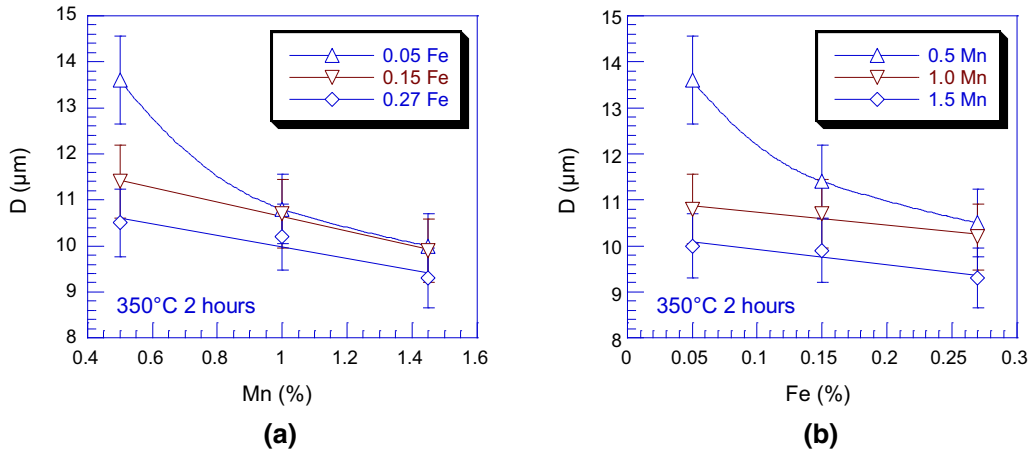

Fig. 8—The mean grain size after batch annealing as a function of (*a*) Mn level and (*b*) Fe level.

Figure 13, both YS and UTS decrease with the increasing temperature and the work hardening is very limited. However, above 500 °C there is a tendency for increase in strength in Alloys-1, 4, and 7, where abnormal dynamic grain growth occurs due to the low Mn level. The optimum testing temperature is around 475 °C for maximum EL, and the EL decreases drastically above 500 °C for Alloys-1, 4, and 7 (Figure 14). In Figures 15, 16, 17, and 18, the high temperature YS and EL are plotted against the Mn and Fe levels. It is obvious that an increasing Mn reduces the YS and increases the EL significantly. Although the effect of Fe on YS is ambiguous, an increasing Fe reduces EL except for the case where Mn is only 0.5 pct.

E. *High Temperature Fracture and Cavitation*

The high temperature tensile fracture is not very dependent on the testing temperature, except for Alloys-1, 4, and 7, where abnormal dynamic grain growth happens at 500 °C to 525 °C. Two types of fracture have been observed: the fracture due to unstable plastic flow and the pseudo-brittle fracture. In general, the alloys with low Mn and Fe fail by unstable plastic flow,

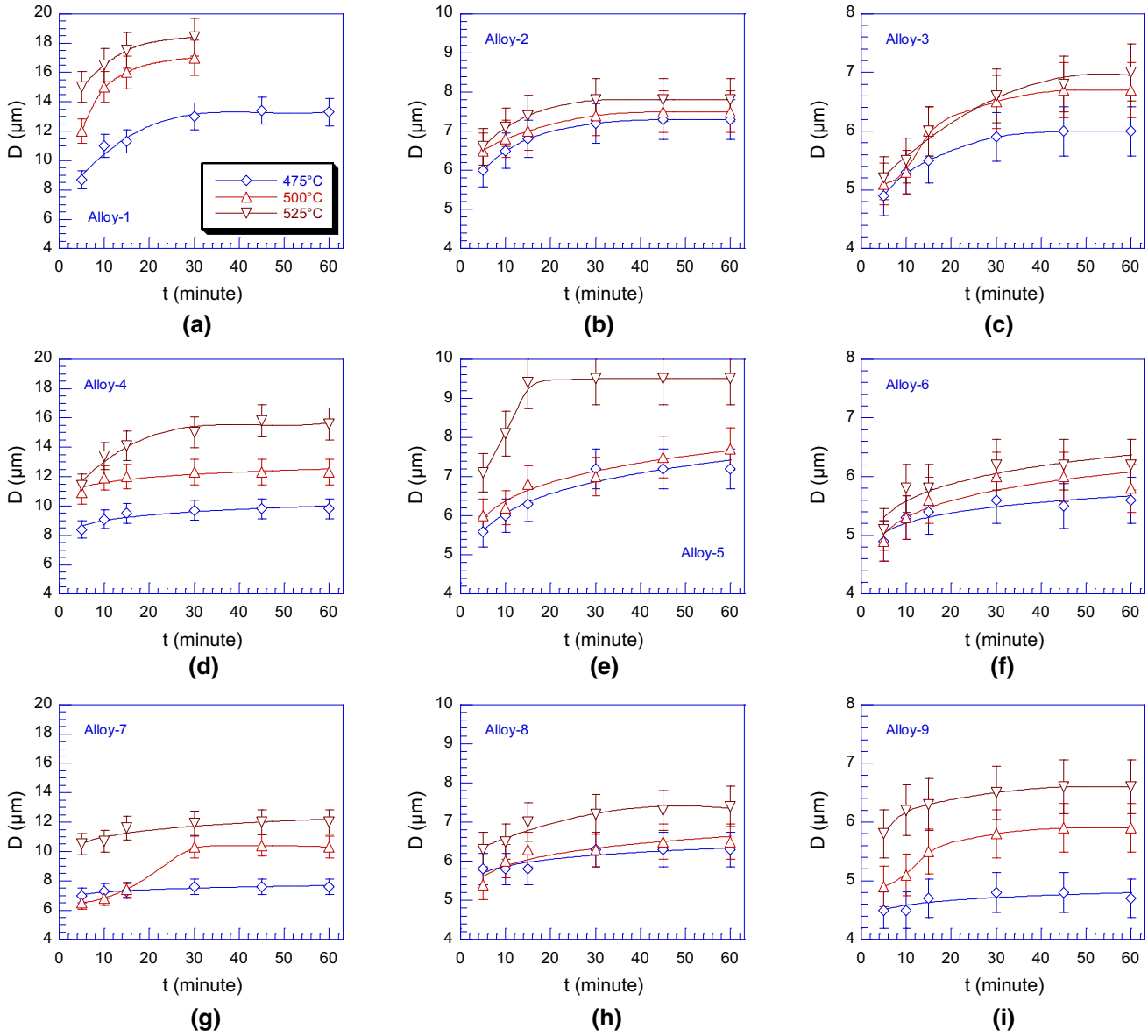

Fig. 9—The mean grain size as a function of the flash annealing time at 475 °C to 525 °C, (*a*) Alloy-1 with 0.52 pct Mn and 0.04 pct Fe, (*b*) Alloy-2 with 0.99 pct Mn and 0.05 pct Fe, (*c*) Alloy-3 with 1.44 pct Mn and 0.05 pct Fe, (*d*) Alloy-4 with 0.51 pct Mn and 0.14 pct Fe, (*e*) Alloy-5 with 0.99 pct Mn and 0.16 pct Fe, (*f*) Alloy-6 with 1.48 pct Mn and 0.18 pct Fe, (*g*) Alloy-7 with 0.51 pct Mn and 0.26 pct Fe, (*h*) Alloy-8 with 0.95 pct Mn and 0.27 pct Fe, and (*i*) Alloy-9 with 1.45 pct Mn and 0.28 pct Fe. For Alloy-1 where abnormal grain growth occurs, the grain size was measured in fine grained region only.

drawing the specimen out to a fine point. As the Mn and Fe, especially the Fe, increase, the fracture tends to the pseudo-brittle type, where the fracture surface is abrupt without obvious necking. Although there is no direct relationship between the type of fracture and the total tensile elongation, an alloy which has a thermally stable fine grain structure, *e.g.*, Alloy-3, yields both better tensile elongation and no pseudo-brittle fracture.

Extensive cavitation has been observed in all the alloys after high temperature tensile testing. Figure 19 shows the volume fraction of cavities as a function of the true strain at 475 °C. The volume fraction increases very slowly from 0 to 2 to 4 pct below a critical strain level, but it increases drastically afterwards. The fracture happens when the volume fraction of cavities reaches 10 to 16 pct. It appears that the critical strain level for rapid cavitation is a function of the Mn and Fe levels, *i.e.*, higher Mn increases the critical strain level while higher Fe reduces it. The cavities, pre-existent or newly generated upon forming, are mostly observed to nucleate around coarse particles in the grain boundaries. Figure 20 shows an example of cavitation development during high temperature tensile testing. In the early stage the volume fraction of cavities increases slowly, and the cavities appear small, spherical, and relatively evenly distributed (Figure 20(a)). Beyond the critical strain level, the cavities become angular in the grain boundaries and triple junctions, and coalescence and inter-linkage are observed (Figure 20(b)). When approaching fracture very extensive coalescence and

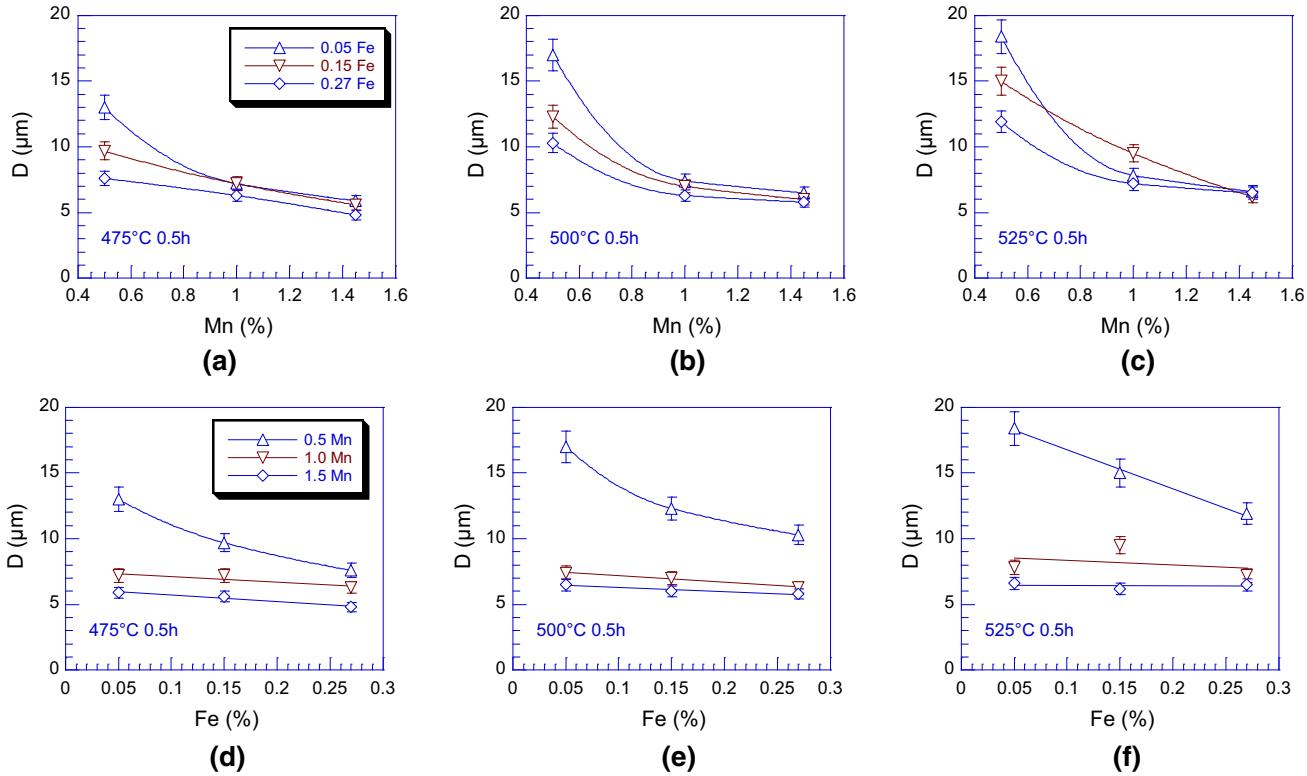

Fig. 10—The saturated mean grain size after flash annealing as a function of the Mn and Fe levels, (*a*) to (*c*) the grain size *vs* Mn after 475 °C, 500 °C, and 525 °C for 30 min, and (*d*) to (*f*) the grain size *vs* Fe after 475 °C, 500 °C, and 525 °C for 30 min.

Table IV. The Mean Grain Size Measured in the Specimen End After Tensile Testing at 425 °C to 525 °C

Alloy	425 °C (μm)	450 °C (μm)	475 °C (μm)	500 °C (μm)	525 °C (μm)
1	9.0	10.0	12.3	a.g.g.	a.g.g.
2	8.1	9.4	9.6	10.8	12.3
3	5.9	6.1	7.7	8.1	8.8
4	8.8	9.2	10.3	10.7	16.0
5	6.2	8.5	9.2	10.4	10.8
6	5.1	5.7	6.1	6.8	7.6
7	8.4	9.0	9.2	10.3	12.0
8	7.4	7.6	8.8	9.9	10.7
9	4.5	4.8	5.9	6.6	7.4

a.g.g. abnormal grain growth.

Table V. The Mean Grain Size Measured in the Specimen Gauge Near Fracture After Testing at 425 °C to 525 °C with Strain Rate of 2×10^{-3} s^{-1}

Alloy	425 °C (μm)	450 °C (μm)	475 °C (μm)	500 °C (μm)	525 °C (μm)
1	6.5	9.2	15.7	a.g.g.	a.g.g.
2	5.3	6.4	8.0	12.7	14.5
3	5.7	6.7	6.7	7.6	8.3
4	8.7	9.8	13.4	a.g.g.	a.g.g.
5	6.2	6.5	7.2	11.6	13.0
6	5.1	5.9	5.3	7.8	8.5
7	7.1	10.2	10.9	a.g.g.	a.g.g.
8	6.5	6.5	7.2	8.5	16.2
9	5.7	6.4	6.7	7.8	8.5

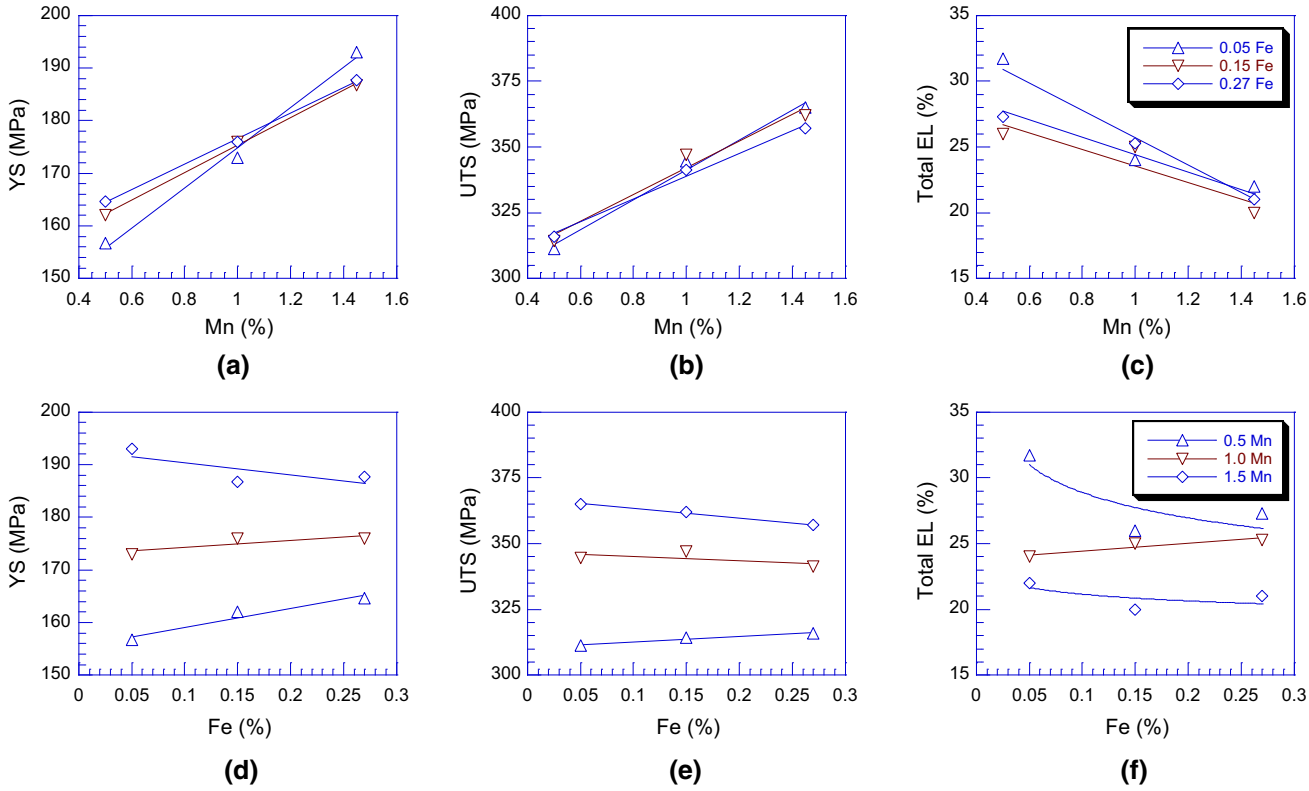

Fig. 11—The room temperature tensile properties of the O temper sheets as a function of Mn and Fe levels, (*a*) to (*c*) YS, UTS, and EL *vs* Mn, and (*d*) to (*f*) YS, UTS, and EL *vs* Fe.

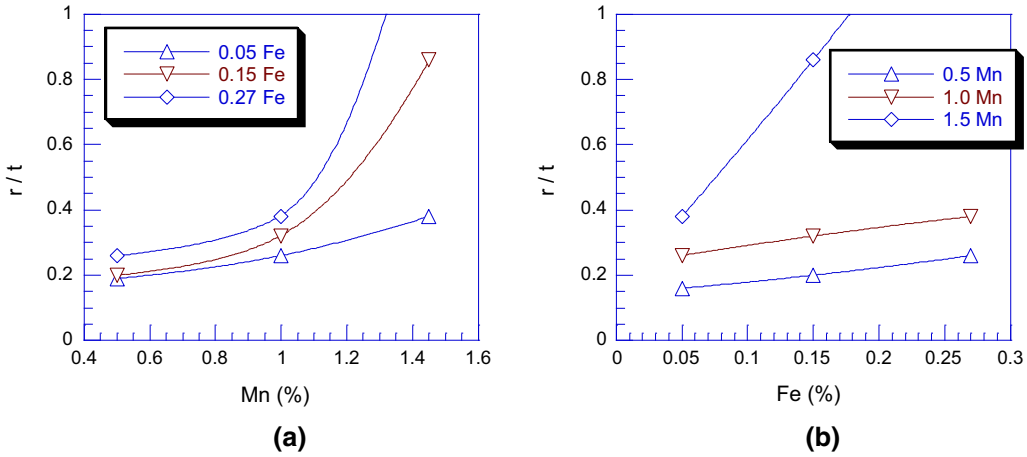

Fig. 12—The wrap bendability of the O temper sheets as a function of (*a*) Mn level and (*b*) Fe level. Alloy-9, having the maximum Mn and Fe, could not pass the mandrel with the largest radius, 3.0 mm, so its $\frac{r}{t}$ is over 2.

inter-linkage of cavities occur, leading to grain boundary failure (Figure 20(c)).

IV. DISCUSSION

A. *Intermetallic Particles*

The present work shows that the effects of Mn and Fe on the mechanical properties of high-Mg aluminum alloys can be attributed to the formation of intermetallic particles, which results in grain refinement and cavitation. In Al-Mg-Mn-Fe-Si system, the possible intermetallic phases include $Al_6(Mn,Fe)$, α-$Al_{15}(Mn,Fe)_3Si_2$, and Mg_2Si for regular DC casting. Since Si was tightly controlled under 0.07 pct in the present work, the α-$Al_{15}(Mn,Fe)_3Si_2$ and Mg_2Si particles are very limited and their effects on grain refinement and cavitation are thus negligible. The coarse $Al_6(Mn,Fe)$ constituents are formed during casting, while the small dispersoids are formed during casting, homogenization, and the early

Table VI. The High Temperature Tensile YS at 425 °C to 525 °C with Strain Rate of 2×10^{-3} s^{-1}

Alloy	425 °C (MPa)	450 °C (MPa)	475 °C (MPa)	500 °C (MPa)	525 °C (MPa)
1	25.5	16.9	14.8	10.0	17.3
2	18.5	10.4	10.7	6.2	6.8
3	11.8	9.1	7.3	5.0	4.4
4	16.9	13.2	11.3	18.0	17.2
5	14.7	7.0	6.9	6.0	6.4
6	13.8	6.8	8.7	4.8	5.2
7	17.5	12.1	11.3	13.3	12.7
8	14.9	9.7	9.5	7.0	5.0
9	15.2	6.5	6.5	5.6	4.1

Table VII. The High Temperature UTS at 425 °C to 525 °C with Strain Rate of 2×10^{-3} s^{-1}

Alloy	425 °C (MPa)	450 °C (MPa)	475 °C (MPa)	500 °C (MPa)	525 °C (MPa)
1	26.7	18.3	16.1	11.6	19.3
2	20.7	11.4	12.0	7.4	7.6
3	15.2	11.1	9.1	7.1	5.7
4	21.1	15.0	13.4	18.8	17.2
5	17.2	10.9	11.0	7.4	7.9
6	16.6	8.8	11.5	5.9	6.0
7	19.8	13.8	13.4	15.3	13.6
8	16.3	10.7	10.1	8.6	7.2
9	16.6	9.6	9.2	7.7	7.2

Table VIII. The High Temperature Tensile EL at 425 °C to 525 °C with Strain Rate of 2×10^{-3} s^{-1}

Alloy	425 °C (Percent)	450 °C (Percent)	475 °C (Percent)	500 °C (Percent)	525 °C (Percent)
1	230	254	205	239	65
2	349	317	340	270	278
3	372	412	451	412	388
4	254	286	286	120	73
5	262	302	294	262	254
6	294	388	357	317	325
7	254	230	231	128	105
8	254	262	254	270	239
9	286	317	301	285	294

stages of hot rolling. Although both Mn and Fe contribute to the formation of Al_6(Mn,Fe) phase, their effects are different. As shown in Figure 3, an increasing Mn increases the density and volume fraction but reduces the particle size, while Fe prefers to form very coarse and irregular-shaped constituents, increasing the particle size and volume fraction but reducing the density.

All the particles help to control the grain structure during recrystallization and grain growth. The constituents and relatively large dispersoids above a critical size increase the nucleation rate by particle-stimulated nucleation (PSN),[26,27] while the fine dispersoids prevent grain growth by Zener pinning.[28] The resultant grain refinement leads to the strength increase at room temperature by grain boundary hardening, but decrease by grain boundary softening in the SPF temperature range, which is above the equicohesive point.[29,30] The combination of increased room temperature strength and decreased high temperature strength is beneficial to SPF, because it reduces the forming load while improves the service strength. The relationship between intermetallic phase and formability is much more complex, since not only the grain structure but also cavitation is involved.

B. *Grain Structures*

In heavily cold-rolled high-Mg aluminum alloys, nucleation of new grains preferentially happens in coarse intermetallic particles and shear bands, while the first one is more dominant. For a given strain level there is a critical particle size for PSN,[26,27] which is around 0.5 to 1 μm in heavily cold-rolled high-Mg aluminum alloys, *e.g.*, AA5083 H18. For site-saturated nucleation, where every particle over the critical size acts as a nucleus, the recrystallized grain size (D_{PSN}) can be estimated by

$$D_{PSN} = d_{PSN} F_V^{-\frac{1}{3}}, \quad [1]$$

where d_{PSN} is the mean size and F_V is the volume fraction of particles over the critical size.[26,27,31] Using the values of d_{PSN} and F_V in Table II, the grain size D_{PSN} is calculated by Eq. [1] for each alloy and the results are listed in the same table. The calculation agrees with the experimental observation that higher Mn and/or Fe make the grain structure finer, but the calculated values are somewhat lower than the experimental data. This is likely due to the fact that grain growth is not accounted for in the equation, so D_{PSN} can only be considered as the lower limit of grain size.

Although dispersoids smaller than the critical size do not contribute to PSN, they determine the stabilized grain size, *i.e.*, the upper limit of grain size, by providing Zener pining on grain boundary migration. The Zener pinning effect is specifically important for SPF, since the forming temperature is quite high. The Zener limit grain size (D_Z) is given by

$$D_Z = \frac{2d_Z}{3F_{VZ}}, \quad [2]$$

where d_Z is the mean size and F_{VZ} is the volume fraction of the fine dispersoids.[28,31] Although no enough data were collected for quantitative analysis, it is indicated by TEM examination that an increasing Mn increases the density and volume fraction of Mn-bearing dispersoids without significantly changing the particle size. A combination of similar d_Z and increasing F_{VZ} makes the D_Z smaller, so the stabilized grain size decreases with increasing Mn, as confirmed experimentally in Figure 9.

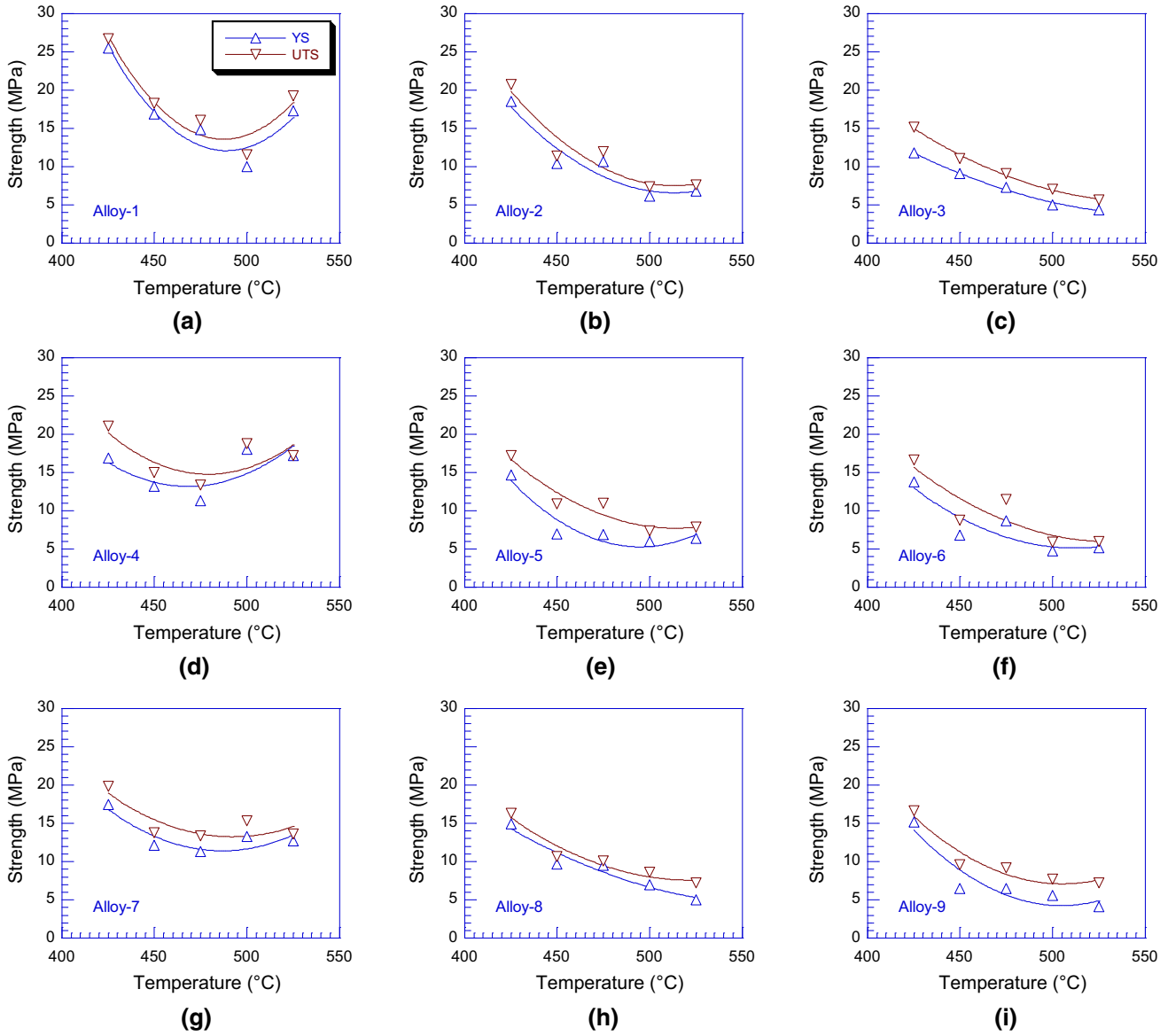

Fig. 13—The high temperature tensile strength as a function of the testing temperature, (*a*) Alloy-1 with 0.52 pct Mn and 0.04 pct Fe, (*b*) Alloy-2 with 0.99 pct Mn and 0.05 pct Fe, (*c*) Alloy-3 with 1.44 pct Mn and 0.05 pct Fe, (*d*) Alloy-4 with 0.51 pct Mn and 0.14 pct Fe, (*e*) Alloy-5 with 0.99 pct Mn and 0.16 pct Fe, (*f*) Alloy-6 with 1.48 pct Mn and 0.18 pct Fe, (*g*) Alloy-7 with 0.51 pct Mn and 0.26 pct Fe, (*h*) Alloy-8 with 0.95 pct Mn and 0.27 pct Fe, and (*i*) Alloy-9 with 1.45 pct Mn and 0.28 pct Fe.

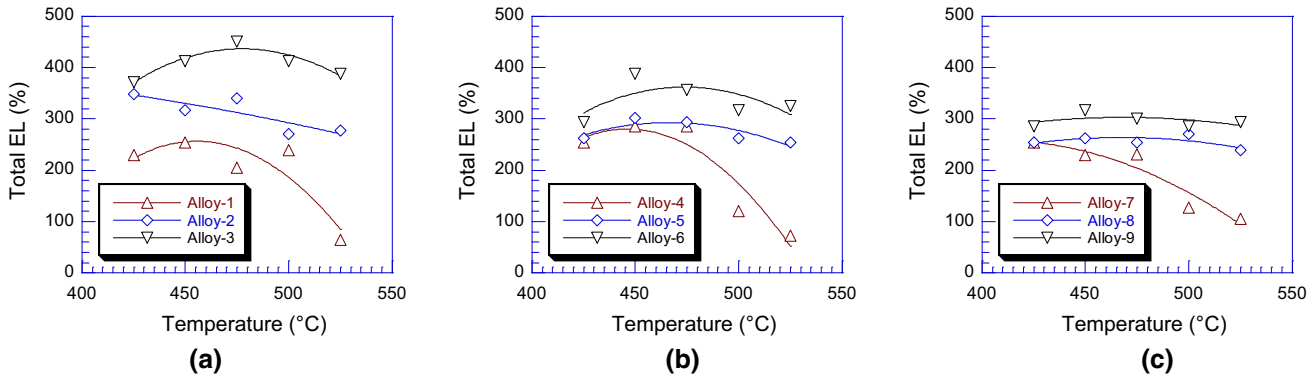

Fig. 14—The maximum high temperature tensile elongation as a function of the testing temperature, (*a*) Alloys- 1 to 3, (*b*) Alloys-4 to 6, and (*c*) Alloys-7 to 9.

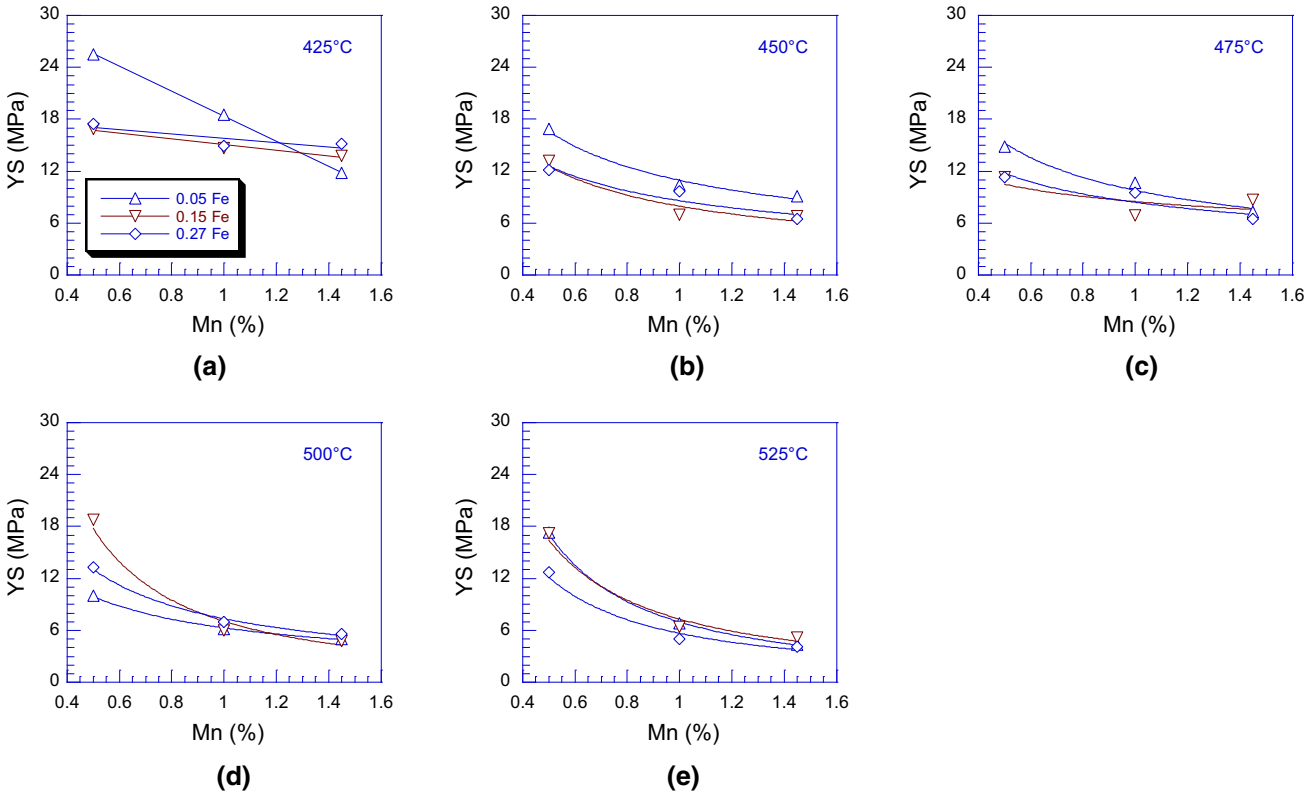

Fig. 15—The high temperature tensile YS as a function of the Mn level at (*a*) 425 °C, (*b*) 450 °C, (*c*) 475 °C, (*d*) 500 °C, and (*e*) 525 °C.

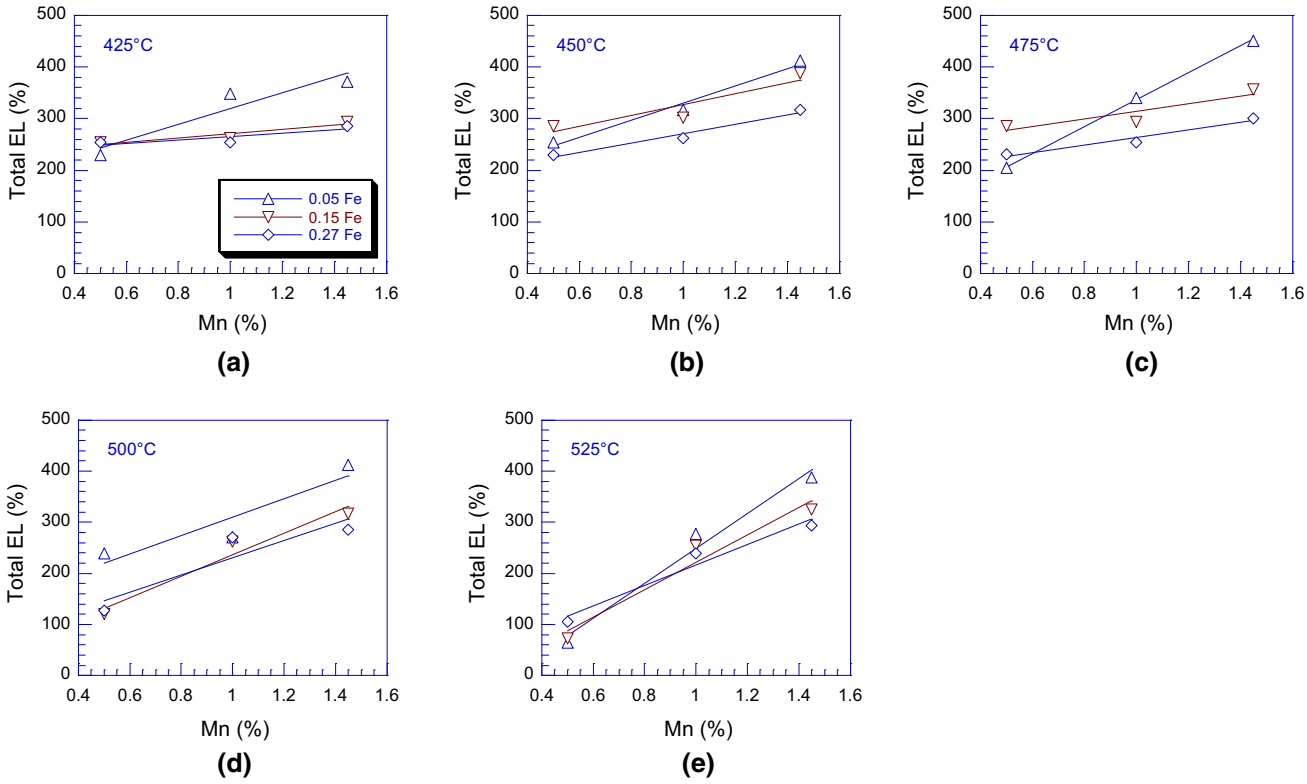

Fig. 16—The maximum high temperature tensile elongation as a function of the Mn level at (*a*) 425 °C, (*b*) 450 °C, (*c*) 475 °C, (*d*) 500 °C, and (*e*) 525 °C.

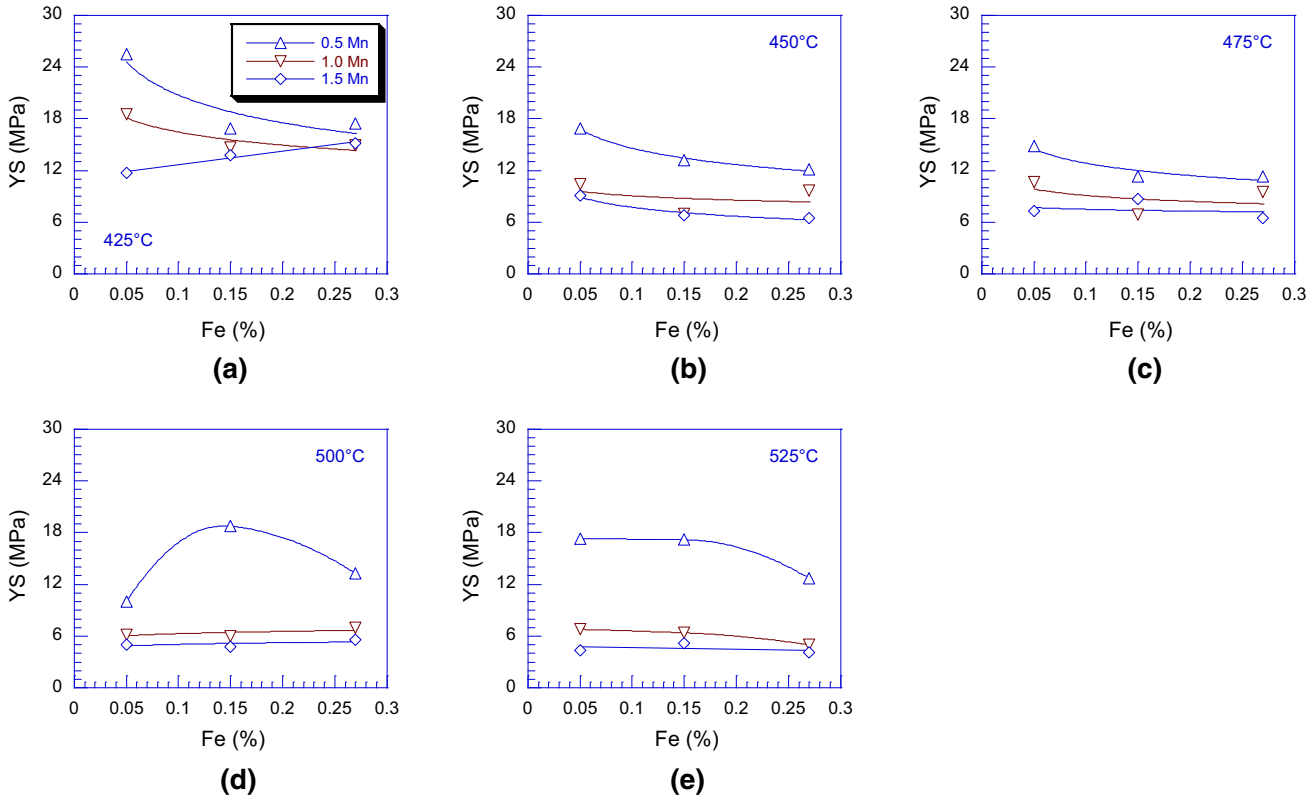

Fig. 17—The high temperature tensile YS as a function of the Fe level at (*a*) 425 °C, (*b*) 450 °C, (*c*) 475 °C, (*d*) 500 °C, and (*e*) 525 °C.

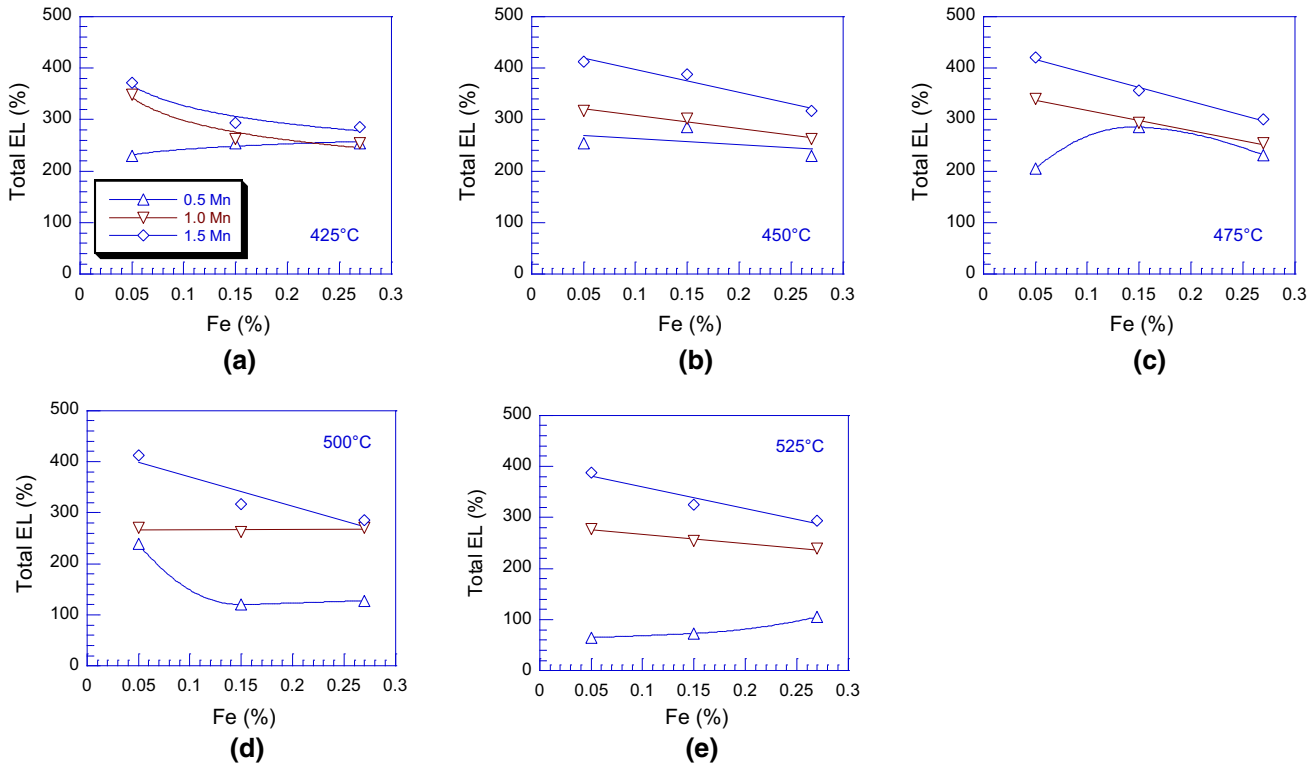

Fig. 18—The maximum high temperature tensile elongation as a function of the Fe level at (*a*) 425 °C, (*b*) 450 °C, (*c*) 475 °C, (*d*) 500 °C, and (*e*) 525 °C.

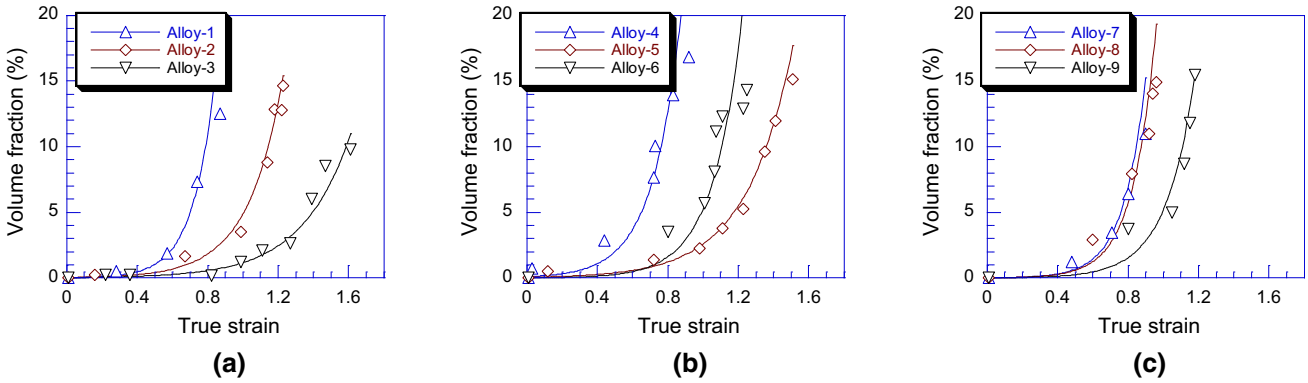

Fig. 19—The volume fraction of cavities as a function of the true strain in tensile testing at 475 °C, (*a*) Alloys- 1 to 3, (*b*) Alloys-4 to 6, and (*c*) Alloys-7 to 9.

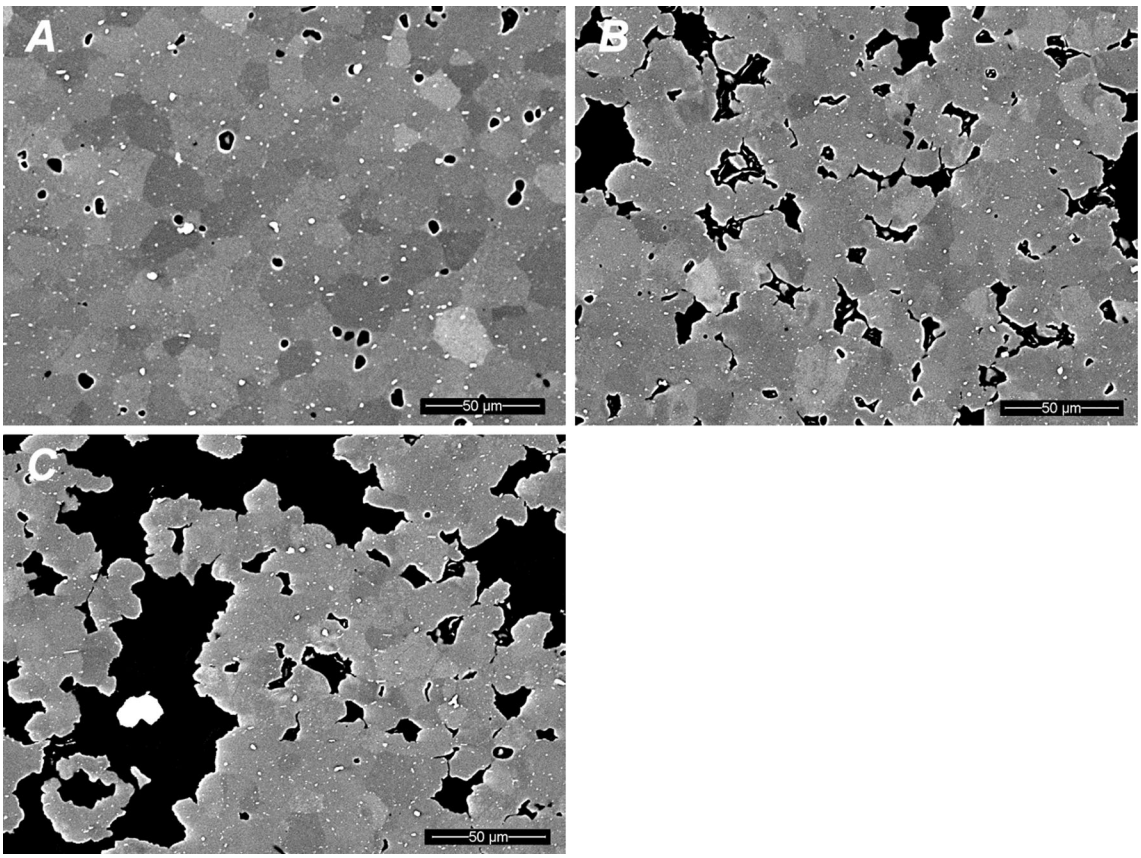

Fig. 20—The SEM backscatter images showing the development of cavitation in Alloy-1 with 0.52 pct Mn and 0.04 pct Fe, (*a*) nucleation and growth of spherical cavities, (*b*) coalescence and inter-linkage of cavities along the grain boundaries, and (c) extensive coalescence and inter-linkage of cavities leading to grain boundary opening.

Upon straining at elevated temperatures, the driving force for grain growth comes from not only the grain boundary tension but also the newly generated dislocations, so grain growth may occur more extensively. Comparing Tables IV and V, it appears that dynamic grain growth is promoted by higher temperature and lower Mn level, *i.e.*, lower Zener pinning effect. When the Mn level is very high, *e.g.*, in Alloys-3, 6, and 9, the grain sizes are independent of strain, indicating that there is little dynamic grain growth. On the contrary, in Alloys-1, 4, and 7 where the Mn level is low, very serious dynamic abnormal grain growth occurs at above 500 °C due to the limited Zener pinning.

C. *Cavitation and Premature Failure*

Having high work hardening at room temperature and high strain rate sensitivity in the SPF temperature range, high-Mg aluminum alloys should be very ductile at all temperatures. However, the high ductility is

seldom realized in commercial sheet products, due to the existence of non-deformable intermetallic particles. During forming, the elastic particles in the aluminum matrix accumulate local strain gradients at the particle–matrix interface due to plastic incompatibility, leading to the separation of particle–matrix interface. The formation, growth, and linkage of cavities eventually result in premature failure. In general, cavitation occurs whenever it is energetically favorable, *i.e.*, when the elastic energy released by a cavity opening is larger than the energy to create the cavity surface. At room temperature, while diffusion-induced plastic relaxation is negligible, the energy for nucleation of a cavity (E_n) on a particle with diameter (d) can be expressed by an inverse relationship, for example,

$$E_n = \frac{4\sigma_C \lambda b}{Cd}, \qquad [3]$$

where σ_C is the interfacial strength, b, the Burgers vector, λ, the length of dislocation pile-up, which is approximately equal to half of the particle spacing, and C, a constant.[32,33]

In principle, cavitation is determined by the local deformation state rather than the macroscopic plastic strain, but it is reasonable to assume that for a given alloy a higher macroscopic strain leads to a higher elastic energy in the vicinity of non-deformable particles. Supposing that cavity nucleation energy E_n is proportional to the macroscopic strain level, *e.g.*, the tensile strain (ε), the critical particle size (d_C) that is able to initiate cavitation should roughly be inversely proportional to the applied strain level, *i.e.*,

$$d_C \propto \frac{1}{\varepsilon} \qquad [4]$$

In the present work, no attempt was made to calculate d_C for a given tensile strain level, because many parameters are difficult to determine, *e.g.*, the interfacial strength σ_C between $Al_6(Mn,Fe)$ and aluminum. However, it has been reported that the critical particle size to nucleate cavities could be as low as ~ 0.01 μm. For example, Tanaka *et al.*[33] indicated that for Si particles in an iron matrix the critical particle size is only 0.01 to 0.1 μm for a plastic strain level of 0.05 to 0.2, while Atkinson[34] observed cavities nucleated at submicron SiO_2 particles in copper single crystals with ~ 5 pct strain by TEM. Assuming the critical particle size is ~ 0.1 μm, most of the $Al_6(Mn,Fe)$ particles are effective nuclei for cavitation at room temperature with more than 20 pct tensile elongation. This is confirmed by the observation in the present work that spherical voids with less than 100 nm diameter were generated at the ends of the long axis of rod-shaped particles, where local strain concentration may occur in cold rolling (Figure 6).

At SPF temperatures, while dislocation mobility by climb is very high, plastic relaxation is extensive and local work hardening is negligible. The nucleation of cavities on intermetallic particles is controlled by diffusion and it is much more difficult to occur than at room temperature. The critical particle size has to be larger than the diffusion length (L) over which stress concentration can be relaxed. There are many mathematical expression of the diffusion length, but the simplest one is by Stowell:[35]

$$L = \left[\frac{11.5\sigma\Omega\delta D_{GB}}{\alpha D\dot{\varepsilon}kT}\right]^{\frac{1}{2}}, \qquad [5]$$

where σ is the stress level, Ω, the atomic volume, δD_{GB}, the product of the grain boundary width and boundary diffusion coefficient, α, the fraction of the total tensile strain accommodated by grain boundary sliding, D, the mean grain size, $\dot{\varepsilon}$, the strain rate, k, the Boltzmann constant (1.38×10^{-23} J K^{-1}), and T, the absolute temperature. Frost has collected the critical parameters for pure aluminum: $\Omega = 1.66 \times 10^{-2}\ nm^3$, $\alpha = 0.6$, and δD_{GB} was given by

$$\delta D_{GB} = 5 \times 10^{-14} \exp\left(\frac{-84 \times 10^3}{RT}\right), \qquad [6]$$

where R is the gas constant (8.3 J mol^{-1} K^{-1}).[36]

Using the UTS values in Table VII for σ and the mean grain size in Table IV for D, the diffusion lengths calculated by Eq. [5] are 0.9 to 1.6 μm at 425 °C to 525 °C with $\dot{\varepsilon} = 2 \times 10^{-3} s^{-1}$ (Table IX). Although the calculation is an approximation only, it indicates that the critical particle size for high temperature cavitation is of the same order as the critical particle size for PSN, and the small particles, which are nuclei for room temperature cavitation, are no longer effective. There is a minimum radius (r^*) for cavities to grow under an applied tensile stress (σ), given by

$$r* = \frac{2\gamma}{\sigma - P}, \qquad [7]$$

where γ is the surface energy and P is the superimposed pressure. The r^* is usually around 100 nm and the voids below it will shrink by the capillarity effect in SPF.[13,37] Therefore, the very small voids generated at the ends of the long axis of rod-shaped particles during cold rolling, as shown in Figure 6, are unlikely to grow in high temperature tensile testing.

Table IX. The Diffusion Length, *i.e.*, The Critical Particle Size for the Initiation of Cavities at 425 °C to 525 °C with Strain Rate of 2×10^{-3} s^{-1}

Alloy	425 °C (μm)	450 °C (μm)	475 °C (μm)	500 °C (μm)	525 °C (μm)
1	1.1	1.1	1.2	—	—
2	1.0	0.9	1.1	1.0	1.2
3	1.0	1.1	1.1	1.2	1.2
4	1.0	1.0	1.2	1.7	1.6
5	1.1	0.9	1.1	1.1	1.3
6	1.2	1.0	1.4	1.2	1.3
7	1.0	1.0	1.2	1.5	1.6
8	1.0	1.0	1.1	1.2	1.2
9	1.2	1.2	1.3	1.3	1.5

D. *Improvement of Superplasticity*

The deformation mechanisms in high-Mg aluminum alloys at room and SPF temperatures are very different. At room temperature the deformation is controlled by dislocation activities, but in SPF temperature range, by both dislocation activity and grain boundary sliding.[38–41] Considering the grain structure, strain rate, and testing temperature range of 425 °C to 525 °C in the present work, it is likely that the deformation mechanisms active at high temperature tensile testing span both the solute drag creep and grain boundary sliding regimes.[41] The non-directional cavitation shown in Figure 20 indicates that grain boundary sliding is more dominant. Accordingly, there are different microstructural requirements to improve the formability at different temperatures. For room temperature formability, the grain structure is not very critical, although a uniform and equiaxed grain structure with moderate grain size is favorable. The intermetallic phases are much more important and it is essential to limit the number of both the coarse and fine particles. On the contrary, for SPF a uniform fine grain structure which is thermally stable at the forming temperature is the most critical,[42] so it is essential to have a certain amount of coarse particles for PSN and a high level of fine particles for Zener pinning.[25–27]

The mechanical properties of a high-Mg aluminum alloy are highly affected by the intermetallic particles, *i.e.*, the Mn and Fe levels. Both the increase at room temperature and the decrease at SPF temperatures of the strength are simply due to the grain refinement effect from $Al_6(Mn,Fe)$ phase. A combination of a high room temperature strength and a low high temperature one is beneficial to SPF, because it reduces the forming load but improves the service strength after SPF. However, due to the different deformation mechanisms, it is very difficult to optimize the room temperature formability and high temperature one at the same time, because the microstructural requirements, especially in regards to the non-deformable intermetallic particles, are opposite. For room temperature formability both coarse constituents and fine dispersoids are responsible for the cavitation-induced premature failure, while at SPF temperatures only the coarse particles, mostly the constituents, are critical. Therefore, to improve superplasticity, Mn has to be maximized and Fe be minimized, but the maximization of Mn unavoidably reduces the room temperature formability.

V. CONCLUSION

(1) In the Al-Mg system, the Mn and Fe form $Al_6(Mn,Fe)$ coarse constituents and fine dispersoids which refine the grain structure by PSN and Zener pinning. The resultant fine grain size makes the strength increase at room temperature but decrease at the SPF temperature range. The increased Mn reduces the formability at room temperature but improves the high temperature formability significantly, while Fe tends to damage the formability at all temperatures.

(2) Due to the different forming mechanisms, it is very difficult to realize high formability at both the room and SPF temperatures. For room temperature formability, both the coarse and fine intermetallic particles should be tightly controlled, because they facilitate premature failure by cavitation. On the other hand, for SPF it is essential to have a certain amount of coarse particles for PSN and a high level of fine particles for Zener pinning, but the very coarse and irregular-shaped constituents are always detrimental.

(3) A combination of high Mn and low Fe is beneficial for high temperature formability, while low levels of both elements are good for cold forming. The superplasticity of high-Mg aluminum alloys is therefore able to be significantly improved by modifying the chemical composition with sacrifice of some room temperature formability. An ideal high-Mg aluminum alloy dedicating to room temperature performance would contain low to moderate Mn and very low Fe, while the one for SPF requires very high Mn and very low Fe.

ACKNOWLEDGMENT

The present work was supported by Natural Resources Canada and Transport Canada through P-001969.001. Mrs. C. Bibby is appreciated for TEM specimen preparation.

REFERENCES

1. A.T. Thomas: *Acta Metall.*, 1966, vol. 14, pp. 1363–74.
2. D.J. Lloyd: *Metall. Trans.*, 1980, vol. 11, pp. 1287–94.
3. J.L. Searles, P.I. Gouma, and R.G. Buchheit: *Metall. Mater. Trans. A*, 2001, vol. 32A, pp. 2859–67.
4. Ø. Ryen, O. Nijs, E. Sjölander, B. Holmerdal, H.-E. Ekström, and E. Nes: *Metall. Mater. Trans. A*, 2006, vol. 37A, pp. 1999–2006.
5. K. Kannan, J.S. Vetrano, and C.H. Hamilton: *Metall. Mater. Trans. A*, 1996, vol. 27A, pp. 2947–57.
6. J.S. Vetrano, C.A. Lavender, C.H. Hamilton, M.T. Smith, and S.M. Bruemmer: *Script. Metall. Mater.*, 1994, vol. 30, pp. 565–70.
7. Y. Takayama, S. Sasaki, T. Tozawa, H. Kato, H. Watanabe, and M. Kokubo: *J. Jpn. Inst. Light Met.*, 1999, vol. 49, pp. 378–82.
8. D.H. Bae and A.K. Ghosh: *Acta Mater.*, 2000, vol. 48, pp. 1207–24.
9. R.M. Cleveland, A.K. Ghosh, and J.R. Bradley: *Metall. Mater. Trans. A*, 2003, vol. 34A, pp. 228–36.
10. M.-A. Kulas, W.P. Green, E.M. Taleff, P.E. Krajewski, and T.R. McNelley: *Metall. Mater. Trans. A*, 2005, vol. 36A, pp. 1249–61.
11. L.D. Hefti: *J. Mater. Eng. Perf.*, 2007, vol. 16, pp. 136–41.
12. R. Grimes, M.J. Stowell, and B.M. Watts: *Metals Technol.*, 1976, vol. 3, pp. 154–60.
13. J. Pilling and N. Ridley: *Superplasticity in Crystalline Solids*, Institute of Metals, London, 1989, pp. 159–95.
14. A.J. Barnes, M.J. Stowell, R. Grimes, D.B. Laycock, and B.M. Watts: *Key Eng. Mater.*, 2010, vol. 433, pp. 11–30.
15. R. Kaibyshev, E. Avtokratova, A. Apollonov, and R. Davies: *Script. Mater.*, 2006, vol. 54, pp. 2119–24.

16. A. Smolej, B. Skaza, B. Markoli, D. Klobčar, V. Dragojević, and E. Slaček: *Mater. Sci. Forum*, 2012, vols. 706–709, pp. 395–401.
17. J.A. Wert, N.E. Paton, C.H. Hamilton, and M.W. Mahoney: *Metall. Trans.*, 1981, vol. 12A, pp. 1267–76.
18. N.E. Paton, C.H. Hamilton, J.A. Wert, and M.W. Mahoney: *J. Metals*, 1982, vol. 34, pp. 21–27.
19. M.W. Mahoney and A.K. Ghosh: *Metall. Trans.*, 1987, vol. 18, pp. 653–61.
20. T.R. Bielr, R.S. Mishra, and A.K. Mukherjee: *JOM*, 1996, vol. 48, pp. 52–57.
21. D.L. Holt and W.A. Backofen: *Trans. ASM*, 1966, vol. 59, pp. 755–68.
22. G. Rai and N.J. Grant: *Metall. Trans.*, 1975, vol. 6A, pp. 385–90.
23. R.Z. Valiev and T.G. Langdon: *Metall. Mater. Trans. A*, 2011, vol. 42A, pp. 2942–51.
24. T.G. Langdon: *Acta Mater.*, 2013, vol. 61, pp. 7035–59.
25. H. Jin: *Mater. Sci. Tech.*, 2017, in press.
26. N. Hansen: *Mem. Sci. Rev. Met.*, 1975, vol. 72, pp. 189–203.
27. F.J. Humphreys: *Acta Metall.*, 1977, vol. 25, pp. 1323–44.
28. C.S. Smith: *Trans. Metall. Soc. AIME*, 1948, vol. 175, pp. 15–51.
29. W. Rosenhain and D. Ewen: *J. Inst. Metals*, 1913, vol. 10, pp. 119–39.
30. Z. Jeffries: *Trans. Ame. Inst. Mining. Metal. Eng.*, 1919, vol. 60, pp. 474–76.
31. F.J. Humphreys and M. Hatherly: *Recrystallization and Related Annealing Phenomena*, Pergamon, Oxford, 1995.
32. M.F. Ashby: *Phil. Mag.*, 1966, vol. 14, pp. 1157–78.
33. K. Tanaka, T. Mori, and T. Nakamura: *Phil. Mag.*, 1970, vol. 21, pp. 267–79.
34. J.D. Atkinson: *Fatigue and the Bauschinger Effect in Dispersion-hardened Copper Single Crystals*, Ph.D. Thesis, University of Cambridge, 1973.
35. M.J. Stowell: *Met. Sci.*, 1983, vol. 17, pp. 1–11.
36. H.J. Frost: *Deformation Mechanism Maps*, Ph.D. Thesis, Harvard University, 1974, pp. 132.
37. M.J. Stowell: *Superplastic Forming of Structural Alloys*, TMS-AIME, Warrendale, PA, 1982, pp. 321–36.
38. R.C. Gifkins: *Metall. Trans.*, 1976, vol. 7A, pp. 1225–32.
39. M.F. Ashby and R.A. Verrall: *Acta Metall.*, 1973, vol. 21, pp. 149–63.
40. T.G. Langdon: *J. Mater. Sci.*, 2006, vol. 41, pp. 597–609.
41. J.-K. Chang, E.M. Taleff, and P.E. Krajewski: *Metall. Mater. Trans. A*, 2009, vol. 40A, pp. 3128–37.
42. J.A. Wert: *JOM*, 1982, vol. 34, pp. 35–41.